DOI: 10.61782/fa.2025.0620

FORUM ACUSTICUM EURONOISE 2025

NOISE SOURCE DIRECTION ESTIMATION USING FLOW-SENSING MEMS MICROPHONES

Thomas Röck[1*] **Martin Hagmüller**[2] **Franz Zotter**[1]
[1]Institute of Eletronic Music and Acoustics, University of Music and Performing Arts Graz, 8010 Graz, Austria
[2]Signal Processing and Speech Communication Laboratory, Graz University of Technology, 8010 Graz, Austria

ABSTRACT

Unattended noise monitoring systems can be used to track the sound level over an extensive amount of time and record whenever the level exceeds a threshold. Direction-of-Arrival (DoA) measured with a microphone array can add relevant information about the noise captured.
This paper investigates a prototype application employing novel directional flow-sensing Micro-Electro-Mechanical Systems (MEMS) microphones integrated into a highly compact array for DoA-detecting noise monitoring. Such sensors are supposed to exhibit a consistent directivity over the audible frequency range and to hereby enable frequency-independent DoA estimation for broadband noise sources. An array prototype is designed on an energy efficient micro controller unit (MCU) that runs three different DoA-estimation methods under test.
The resulting prototype uses one omnidirectional and three directional, flow-sensing MEMS microphones. Measurements confirm that a high spatial aliasing limit could be reached without sacrificing low-frequency directivity. Our field study validates applicability to DoA-detecting noise monitoring at cheap computational costs.

Keywords: *Acoustic DoA estimation, MEMS velocity microphone array, ARM microcontroller*

1. INTRODUCTION

Compliance with noise regulations typically requires monitoring acoustic emissions from specific sources and the comparison to legal limits [1]. In unattended noise monitoring systems, the sound level is tracked over a long period of time. When the level surpasses a threshold, the system activates an alarm, requiring a human operator to restore order manually. This is time-consuming, especially if the object to monitor is near roads, railways and airports. Using Artificial Intelligence (AI) for unattended noise monitoring systems allows for the automatic classification of triggering events and potential exclusion from the overall measurement [2, 3]. Deep learning methods are remarkably successful in Sound-Event-Detection (SED). However, the current leading models still encounter errors, especially when having to distinguish between different types of vehicles [4] or distinct soundscapes [5]. However, there is more information than what can be contained in single-channel sound. For instance, Direction-of-Arrival (DoA) offers useful additional information. In particular, DoA allows to limit the solid angle/field of view, within which noise shall be monitored. Current methods in DoA estimation for noise monitoring applications investigate arrays incorporating mainly omnidirectional MEMS microphones. The “Noise Compass” [6] is an array that includes eight omnidirectional MEMS microphones and computes the DoA of the dominant noise source using a Time-Difference-of-Arrival method. Another work proposes the design of a 3D sound intensity probe using eight MEMS pressure microphones on the vertices of a 2cm × 2cm cube [7].
This work investigates the performance of novel directional, flow-sensing MEMS microphones [8, 9] that sense acoustic particle velocity. An orthogonal arrangement of velocity microphones combined with an omnidirectional pressure microphone enables the computation of the three-dimensional pseudo-intensity vector, which indicates the direction of sound propagation and, accordingly, the direction of the sound source emitting the sound field. We derive and compare three DoA-estimation methods applicable to the proposed array geometry, which are implemented on a low-power ARM microcontroller. Additionally, the results of directivity measurements used

*Corresponding author: roeck@iem.at.

to verify the figure-of-eight polar pattern of the velocity microphones are discussed. Finally, we present two case studies to demonstrate the array's performance in the field. The proposed array prototype is suitable for noise DoA-estimation applications and produces good results with minimal signal processing. Drawbacks such as the influence of wind on the velocity microphones should be discussed and addressed.

2. SIGNAL MODEL

We assume an acoustic signal $s(t)$ emitted by a sound source that lies at some distance along the unit DoA vector

$$\boldsymbol{u} = \begin{pmatrix} \cos(\varphi)\cos(\vartheta) \\ \sin(\varphi)\cos(\vartheta) \\ \sin(\vartheta) \end{pmatrix}, \tag{1}$$

where $\varphi \in [0, 2\pi[$ is the azimuth angle and $\vartheta \in [-\frac{\pi}{2}, \frac{\pi}{2}]$ is the elevation angle of the source. For our array with 4 microphones located at the center of a coordinate system, let there be K sources at the directions $\boldsymbol{u}_k$ with the signals $s_k(t)$, and an $\mathbb{R}^{4\times 1}$ signal vector recorded by the array

$$\boldsymbol{x}(t) = \sum_{k=1}^{K} s_k(t)\, \boldsymbol{y}(\boldsymbol{u}_k) + \boldsymbol{v}(t). \tag{2}$$

Here, $\boldsymbol{y}(\boldsymbol{u}) \in \mathbb{R}^{4\times 1}$ is the array manifold vector for a continuous direction $\boldsymbol{u}$, and $\boldsymbol{v}(n) \in \mathbb{R}^{4\times 1}$ is a vector that contains the additive zero-mean self noise of each microphone.
Similar to [10], we assume the following conditions:

A) Incident waves are local plane waves at the array, implying (i) far-field conditions characterized by array-to-source distances much greater than a wavelength, and (ii) array dimensions much smaller than a wavelength to avoid both diffraction and time differences of arrival.
B) Band limitation: The signal is bandlimited accordingly, $\omega_{\min} < \omega < \omega_{\max}$, such that both conditions are fulfilled.

The microphone array in this work follows a WXYZ (B-format) layout with three orthogonal velocity microphones and one omnidirectional pressure microphone. The resulting array manifold vector $\boldsymbol{y}(\boldsymbol{u}) \in \mathbb{R}^{4\times 1}$ is defined as

$$\boldsymbol{y}(\boldsymbol{u}) = \begin{pmatrix} 1 \\ \boldsymbol{u}\sqrt{3} \end{pmatrix}. \tag{3}$$

We further assume consistent microphone directivity within the frequency range of interest, which is why $\boldsymbol{y}(\boldsymbol{u})$ is assumed to be frequency-independent.

3. FLOW-SENSING MEMS MICROPHONE

The Soundskrit directional MEMS microphone is the result of a collaboration between researcher Ronald N. Miles, who has extensively studied sound velocity sensing [11–13], and Stephane Leahy from Soundskrit, who designed a new transducer based on capacitive sensing [8]. The sensing element consists of multiple porous plates, fixed beams, and cantilevers, creating a highly flexible membrane designed to enhance the influence of air viscosity on its movement due to its material properties. Two port holes on the front and back of the microphone allow sound to flow through the sensing element. In our array prototype as seen in Fig. 1, we incorporate three of Soundskrit's SKR0410 first-generation digital MEMS microphones in an orthogonal alignment. An omnidirectional microphone by Infineon is brought into the center of the array using a Flex PCB. The coupon board PCBs of the velocity microphones are attached to a hollow 3D-printed housing. The distance between the orthogonal microphone and the three velocity microphones is $d = 6.5$ mm, resulting in a maximum microphone distance of $d_{\max} = \sqrt{2}\, d = 9.2$ mm and consequently a minimum aliasing frequency at $\frac{c}{2d_{\max}} = 18657$ Hz where $c = 343$ m/s is the speed of sound.

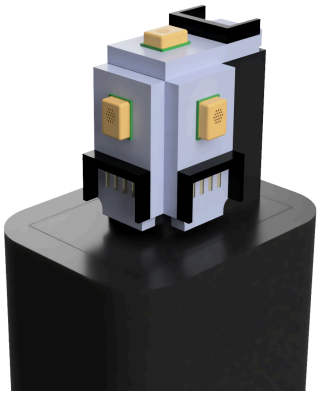

Figure 1: The array prototype. The MEMS velocity microphones are mounted on the white PCB coupon boards. The omnidirectional MEMS microphone is located in the center of the array. The largest distance between any two microphones is 9 mm.

3.1. Directivity measurements of the microphones

The polar pattern of the MEMS velocity microphones is specified as a figure-of-eight (Fo8) and has been verified through directivity measurements. These measurements utilize an array of loudspeakers mounted on a circular frame with radius $r = 1.5\text{m}$ facing the circle's center point where the microphone array specimen is located, as seen in Fig. 2. The array is mounted on a stand on a turntable that rotates the array along the vertical axis in 10° azimuthal steps, resulting in an angular resolution of $\Delta\varphi = 10°$. The elevation resolution is given by the spacing of the loudspeakers, which is $\Delta\vartheta = 11.25°$.

Overlapping exponential sweeps were employed as the measurement signal [14]. The loudspeaker's individual frequency response is equalized by measurements recorded with an *Earthworks* measurement microphone. Spherical surface plots are generated with a MATLAB tool[1] that interpolates the 10° × 11.25° sample grid using 14th-order spherical harmonics and performs far-field extrapolation in the spherical harmonics domain.

We observed a consistent phase difference of approximately 60° between the omnidirectional MEMS and the Fo8 microphones. This difference must be accounted for to prevent a sign flip of the pseudo-intensity vector. Therefore, the Fo8 microphones are equalized to the frequency response of the omnidirectional microphone.

Furthermore, the orthogonal MEMS microphones exhibit an orientation misalignment, especially the X- and Z microphones (as depicted in Fig. 3). Fortunately, this misalignment can be easily corrected through a change of basis transformation

$$\hat{\boldsymbol{u}}' = \boldsymbol{D}\left(\tilde{\boldsymbol{D}}^{\mathrm{T}}\right)^{-1}\hat{\boldsymbol{u}}. \tag{4}$$

This transformation projects the estimated DoA vector onto the inverse of a matrix containing the actual alignment of the microphones, transforming the vector to lie within the orthonormal Cartesian basis. Here, $\boldsymbol{D} = \boldsymbol{I}$ denotes the Cartesian basis which is an identity matrix and $\tilde{\boldsymbol{D}}$ contains the actual alignment of the Fo8 microphones determined by the measurement.

The measured polar pattern of a cardioid beam steered to $\varphi = 90°$ is shown in Fig. 4 a). In this depiction, the magnitude is normalized for each frequency bin as the MEMS microphones are less sensitive at lower frequencies but that sensitive was also not considered in the simulation. However, the directionality and consequently the beampattern is maintained even for lower frequencies. We do observe inconsistencies in the beampattern with frequencies starting at 4000 Hz which could be attributed to temporal measurement errors or acoustic turbulences within the case. The simulated energy response of a cardioid beamformer steered to $\varphi_s = 90°$ and $\vartheta_s = 0°$ is depicted in Fig. 4 b). Initial interference patterns can be observed at $\frac{c}{4d} = 13192$ Hz. Below that frequency, the beamformer consistently favours the steering direction without spatial aliasing.

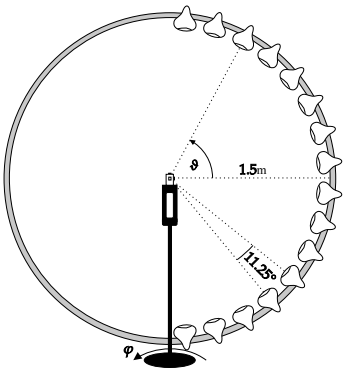

Figure 2: The measurement setup. 16 loudspeakers with a spacing of 11.25°, mounted on a circular frame with radius $r = 1.5\text{m}$, face the microphone array.

[1] https://git.iem.at/p2774/balloon_holo

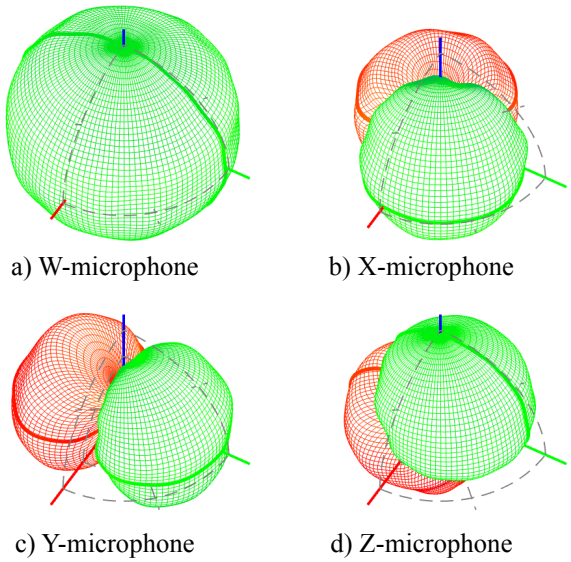

a) W-microphone b) X-microphone

c) Y-microphone d) Z-microphone

Figure 3: Directivity for the W, X, Y, and Z microphone measured at a frequency of 500 Hz. The colors indicate the phase response of the micorphones.

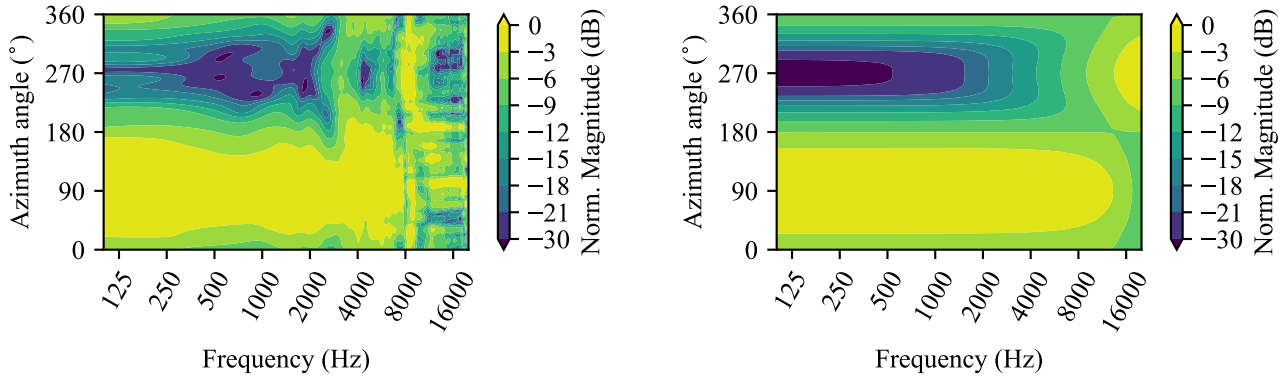

a) Measured polar pattern.

b) Simulated array response.

Figure 4: A cardioid beam (linear combination of the omni- and Fo8 microphones) is steered to a direction of $\varphi = 90°$ and $\vartheta = 0°$. In the measurement in a), the magnitude is normalized per frequency. In reality, the MEMS microphones are less sensitive in the lower frequency range but that sensitivity was also not considered in the simulation depicted in b) which is performed by placing sound sources around the array and evaluating Green's function for planar waves that depends on the distance between the source and receiver.

4. DOA ESTIMATION METHODS

In this section we present three DoA-estimation methods. We extend a simple beamforming approach with a seasoned, well-established subspace algorithm applicable for any kind of array-geometry, followed by a pseudo-intensity method that makes use of the sampling of the sound pressure and velocity vector.

4.1. Steered Response Power (SRP)

The Steered Response Power (SRP) method is fundamentally based on beamforming, utilizing the array response vector $\boldsymbol{y}(\boldsymbol{u})$ as defined in Eqn. (3) and an estimation of the covariance matrix

$$\boldsymbol{C}_{\mathrm{xx}} = \boldsymbol{X}^{\mathrm{T}}\boldsymbol{X} \tag{5}$$

of a N-sample signal block $\boldsymbol{X} \in \mathbb{R}^{N\times M}$. For a set of $\mathcal{G}$ discrete points on the surface of a unit-sphere, sampled using a Fibonacci lattice, we compute

$$P(\boldsymbol{u}) = \boldsymbol{y}^{\mathrm{T}}(\boldsymbol{u})\,\boldsymbol{C}_{\mathrm{xx}}\,\boldsymbol{y}(\boldsymbol{u}). \tag{6}$$

The point that maximizes this power is the estimated direction of arrival

$$\hat{\boldsymbol{u}} = \underset{\boldsymbol{u}\in\mathcal{G}}{\operatorname{argmax}}\, P(\boldsymbol{u}). \tag{7}$$

4.2. Multiple Signal Classification (MUSIC)

Introduced in 1986 [15], MUSIC is a renowned subspace method and extends the aforementioned beamforming technique. It relies on the eigen-decomposition of the covariance matrix $\boldsymbol{C}_{\mathrm{xx}}$ and successive separation of the eigenvectors into a signal- and noise subspace. The signal model claims that the wavefronts received at the M microphones are a linear combination of D incident wavefronts and noise. After the eigendecomposition of the covariance matrix of the signal vector $\boldsymbol{x}$, the D largest eigenvalues and their corresponding eigenvectors span the signal subspace, whereas the eigenvectors corresponding to the $M - D$ smallest, clustered eigenvalues span the noise subspace $\boldsymbol{E}_{\mathrm{n}}$. A pseudo spectrum $\hat{P}_{\mathrm{MU}}(\boldsymbol{u})$ is introduced, which computes to the squared norm of the projection of $\boldsymbol{y}(\boldsymbol{u})$ onto the noise subspace. The direction that maximizes the pseudo spectrum

$$\hat{P}_{\mathrm{MU}}(\boldsymbol{u}) = \frac{1}{\left\|\boldsymbol{E}_{\mathrm{n}}^{\mathrm{T}}\,\boldsymbol{y}(\boldsymbol{u})\right\|^2} \tag{8}$$

is the predicted direction of arrival $\hat{\boldsymbol{u}}$

$$\hat{\boldsymbol{u}} = \underset{\boldsymbol{u}\in\mathcal{G}}{\operatorname{argmax}}\, \hat{P}_{\mathrm{MU}}(\boldsymbol{u}). \tag{9}$$

4.3. Active Intensity Measurement (AIM)

Euler's equation relates the acoustic pressure p to the sound velocity vector $\boldsymbol{v}$

$$-\nabla p = \rho_0 \frac{\partial \boldsymbol{v}}{\partial t} \tag{10}$$

where $\rho_0 \approx 1.2 \frac{\text{kg}}{\text{m}^3}$ is the atmospheric density. For sufficiently far away sources, i.e. plane-wave conditions, the ∇-operator is equal to $\partial(\boldsymbol{u}_\text{s}/c)/\partial t$ and Eqn. (10) becomes

$$\boldsymbol{v} = -\frac{\boldsymbol{u}\, p}{\rho_0 c}. \tag{11}$$

As the B-format signals of a first-order ambisonics microphone are $W = p$ and $[X, Y, Z]^\text{T} = -\rho_o c \sqrt{2}\, \boldsymbol{v}$, the predicted direction by AIM is

$$\begin{aligned} \hat{\boldsymbol{u}} &= -\frac{\rho_0 c\, \boldsymbol{I}}{|p|^2} = -\frac{\rho_0 c\, p \boldsymbol{v}}{|p|^2} = \frac{\rho_0 c\ |p|^2\ \boldsymbol{u}}{\rho_0 c\ |p|^2} = \boldsymbol{u} \\ &= \frac{W\,[X, Y, Z]^\text{T}}{\sqrt{2}\ |W|^2} \end{aligned} \tag{12}$$

and the estimator averaging over one block of samples is

$$\hat{\boldsymbol{u}} = \frac{\mathbb{E}(W[X, Y, Z]^T)}{\sqrt{2}\mathbb{E}(W^2)}. \tag{13}$$

5. HARDWARE IMPLEMENTATION

The microphone array is powered by a *STM32U5A9NJ* ARM microcontroller which also runs the DoA-estimation algorithms and performs 1/1 octave band filtering for eight octave bands with center frequencies from 31.5 Hz - 4000 Hz. The built-in interleaved sampling mode of the Multi-Function-Digital-Filter (MDF) of the ST guarantees precise sampling of the four microphone channels. After acquiring a block of $N = 2048$ samples, that block is filtered eight times by 4$^\text{th}$ order IIR butterworth bandpass filters following the ANSI S1.11-2004 specifications [16], effectively whitening the signal in its respective band. A separate recording mode allows for the transmission of the recordings to a host computer for postprocessing and the results shown in Sec. 6 were obtained by offline analysis of the recordings.

5.1. Computational effort of the algorithms on the chip

The *STM32U5A9NJ* MCU contains a single-core *Cortex-M33* ARM processor operating at a system clock frequency of up to 160 MHz. We benchmarked the algorithms by executing a Monte Carlo simulation comprising 1000 trials and selecting the median number of clock cycles required for the algorithm to finish. We set an external timer to the same system clock rate $f_\text{CLK} = 160$ MHz. Computational improvements could be made using the CMSIS DSP library[2] tailored towards the specific CPU architecture of the *Cortex-M33*.

[2]https://arm-software.github.io/CMSIS_5/DSP/html/index.html

Table 1: Computational effort of the three algorithms for different sample sizes N. The numbers below the algorithm's names denote the number of clock cycles required for the algorithm to finish.

N	SRP	MUSIC	AIM
512	739 384	1 948 476	35 779
1024	808 535	2 039 794	71 133
2048	946 834	2 192 544	141 815

For an efficient processing of the MUSIC algorithm, the property of the covariance matrix $\boldsymbol{C}_\text{xx}$ as real-valued and positive semi-definite was exploited to efficiently use a real-valued Schur decomposition for eigendecomposition $\boldsymbol{C}_\text{xx} = \boldsymbol{E}\,\text{diag}(\boldsymbol{s})\,\boldsymbol{E}^\text{T}$, where $\boldsymbol{E}$ contains all eigenvectors and $\text{diag}(\boldsymbol{s})$ the eigenvalues. The noise subspace $\boldsymbol{E}_\text{n}$ corresponds to the 3 smallest eigenvalues with the signal subspace set to $D = 1$. The number of points for SRP and MUSIC is set to $\mathcal{G} = 1650$ to achieve an angular resolution of approximately $\Delta\boldsymbol{u} = \sqrt{\frac{4\pi}{1650}} \frac{180}{\pi} = 5°$.
Tab. 1 shows the measured clock cycles for different block lengths N. AIM is faster than both MUSIC and SRP, mainly because of their expensive grid search over $\mathcal{G}$ directions. Complexity roughly scales with $\mathcal{O}(N)$ for AIM, in contrast to $\mathcal{O}(N) + \mathcal{O}(\mathcal{G})$ for SRP and MUSIC. The computation of the SRP power spectrum is cheaper than Schur decomposition.

6. CASE STUDIES

Case studies on the array performance in real-world scenarios were carried out, of which two are presented in the following sections. The first scenario demonstrates the array performance on a low-frequency sound source. The second study investigates the influence of wind, which is particularly evident in recordings of the flow-sensing microphones. Direction estimates are performed individually for eight 1/1 octave bands with center frequencies ranging from 31.5 Hz to 4 kHz and additionally for the A-weighted recording. The system's sampling rate is set to 16 kHz. The number of discrete unit vectors $\mathcal{G}$ for SRP and MUSIC is 1650, resulting in an angular resolution of approximately 5°. The number of signals in MUSIC is assumed to be $D = 1$. The individual 5-minute recordings are buffered into blocks of $N = 2048$ samples, each block yielding a direction estimate for segments where a noise source is present with certainty. Given that the true direction of the sound source is unknown, we can only analyse the scattering of direction estimates. For this purpose, we

analyse boxplots containing samples of the angle between an estimate $\hat{\boldsymbol{u}}$ and the mean direction $\boldsymbol{\mu}_{\mathrm{A}}$ of the A-weighted filter bank, i.e. $\arccos(\boldsymbol{u}^{\mathrm{T}}\boldsymbol{\mu}_{\mathrm{A}})$. The boxes in the boxplots shown extend from the first to the third quartile with a line at the median. The whiskers extend from the box to the farthest data point, lying within 1.5 times the interquartile range. Fliers are shown as grey circles. Additionally, histograms counting direction samples estimated by AIM are presented.

6.1. Low-frequency screed silo pump

The first study was conducted next to a construction site during the operation of a silo pump. Free-field conditions could not be fulfilled as the recording area was surrounded by residential houses, as can be seen in Fig. 5. Nevertheless, this example should demonstrate the direction estimation capabilities of the miniature array for low-frequency sources. As can be seen in the spectrogram segment shown in Fig. 6, the silo pump emits a particularly dominant tone at 50 Hz and additional harmonic overtones. For conventional, small-aperture microphone arrays, the accurate detection of a noise source in this frequency range should pose a great challenge. However, as evident in the boxplots presented in Fig. 7, the direction estimates exhibit minimal deviation from the mean direction $\boldsymbol{\mu}_{\mathrm{A}}$ in the 31.5- and 63 Hz frequency bands. Notably, in the 31.5 Hz band, a remarkably precise direction estimate of AIM's histogram for a single frame is discernible in Fig. 8. Comparing the algorithm's performance in this scenario, we can note that SRP, AIM, and MUSIC yield similar estimation outcomes. However, AIM does show greater scattering of its direction estimates in the frequency bands from 250 Hz to 4000 Hz.

Figure 5: In the first scenario, a silo pump next to a construction site in a residential area was recorded.

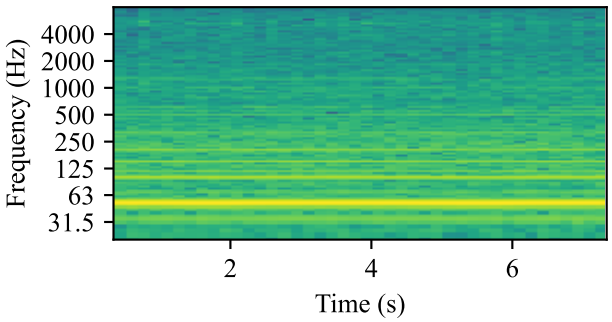

Figure 6: Spectrogram of the pump recording in a segment where an especially dominant low-frequency tone at 50 Hz is present.

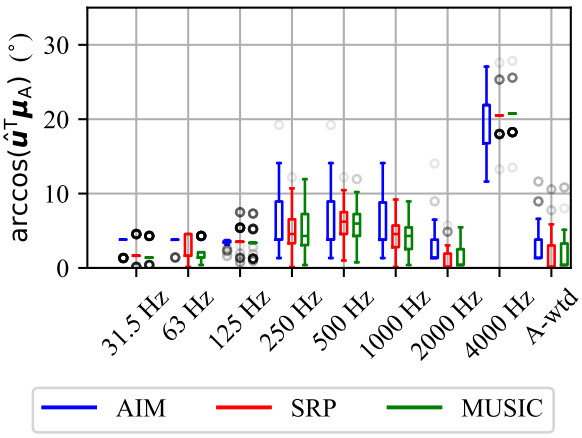

Figure 7: Angle between the direction estimates $\hat{\boldsymbol{u}}$ and the mean direction of the A-weighted filter $\boldsymbol{\mu}_A$ for the silo pump recording.

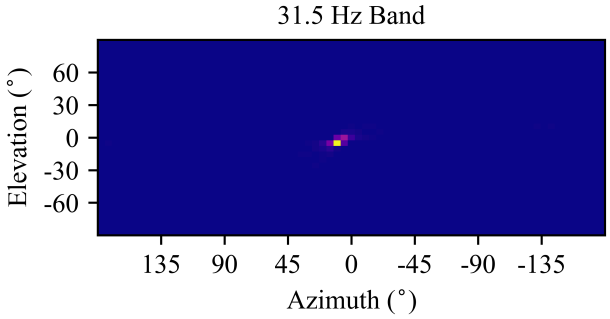

Figure 8: A histogram counting direction estimates for a single block of the silo recording. Computed by AIM, evaluated for the 31.5 Hz octave band.

Such behaviour could be attributed to the reflective recording scenario and, consequently, additive wavefronts from mirror sources, causing more deviations in the per-sample estimates of the pseudo intensity vector. Notably, in the 4000 Hz band, an angular discrepancy of 20° is evident. Further examination of this band revealed that the elevation of the estimation is 20° higher than for $\boldsymbol{\mu}_{\mathrm{A}}$ but with similar azimuth. It is possible that a more prominent noise source, perhaps originating from another point on the silo itself, is present at higher elevations.

6.2. Parked airplane in the presence of wind gusts

For the second study, the array was mounted on a terrace of an airport facing the runway, as shown in Fig. 9. We want to demonstrate the array's performance in non-ideal weather conditions, such as in the presence of wind gusts that interfere with the recording. Occasional wind gusts can be seen in Fig. 10 where they occupy the frequency range of 20 Hz to 100 Hz. We observed that recordings captured by the Fo8, flow-sensing microphones were significantly more influenced by wind compared to recordings captured by the omnidirectional pressure microphone. Evidently, as wind gusts distort the recording, they will deteriorate the performance of the direction estimation. A greater scattering of direction estimates can be seen in Fig. 11, vastly influencing the performance of all algorithms in the 31.5 Hz and 63 Hz band. Turbulent - but optically quite artistic estimations of the direction of the pseudo intensity vector can be appreciated in Fig. 12. This picture further emphasizes the impact of wind at lower frequencies. However, with increasing center frequency, the performance improves for all algorithms. In comparison to the scenario in Sec. 6.1, their prediction performance seems to be even more similar.

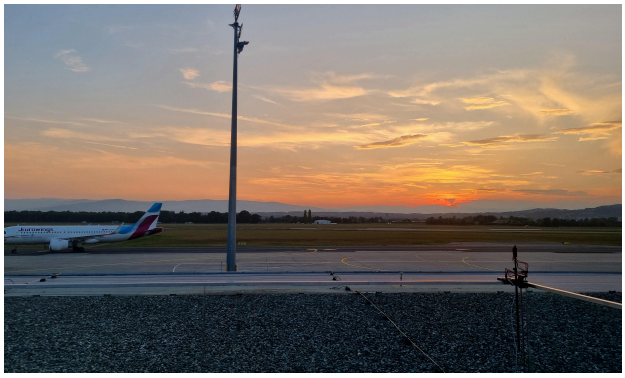

Figure 9: The second recording scenario was conducted at an airport and the sound source was the parked airplane seen on the left.

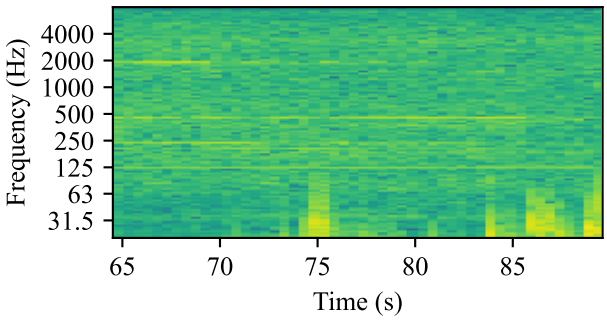

Figure 10: Spectrogram of the airplane source. Occasional wind gusts can be seen occupying the frequency range from 20 Hz to 100 Hz.

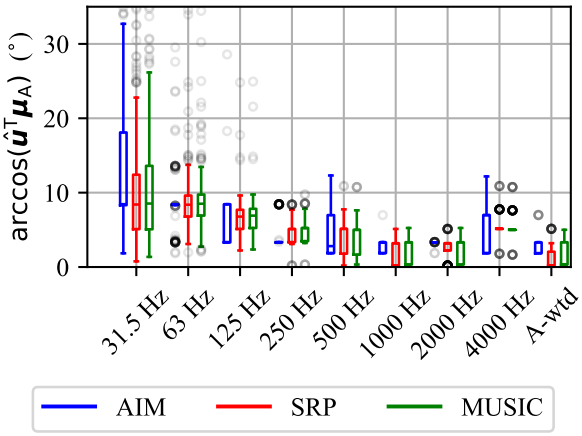

Figure 11: Angle between the direction estimates $\hat{\boldsymbol{u}}$ and the mean direction of the A-weighted filter $\boldsymbol{\mu}_A$ for the airport recording.

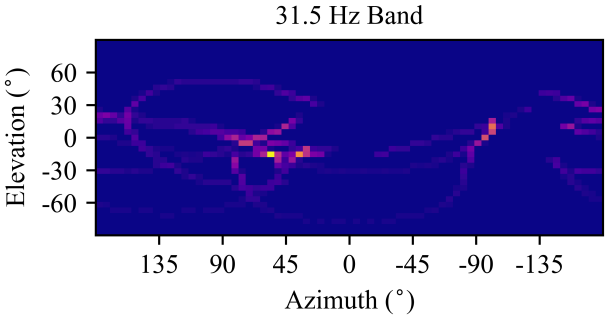

Figure 12: A histogram counting direction estimates computed by the AIM algorithm. Evaluated for the 31.5 Hz octave band for the airplane source.

7. CONCLUSION

We presented a miniature microphone array comprising directional, velocity-sensing MEMS microphones suitable for broadband noise source direction estimation. We verified the individual microphone and array directivities over a broad frequency range, and showed that the small sensor spacing provides a high spatial aliasing frequency limit. For the array prototype, three direction-of-arrival detection algorithms were implemented on an energy-efficient MCU. It was shown that the computational load varied depending on the complexity of the underlying algorithm. Field studies further verified the applicability of the microphone array in real-world scenarios, demonstrating comparable estimation performance for the different algorithms, but also highlighting the influence of wind, primarily on the velocity microphones. Consequently, users should consider their windscreen solution when incorporating flow-sensing microphones. Compared to conventional microphone arrays using non-coincident, omnidirectional sensors, the microphones in this configuration can be brought together as closely as possible without sacrificing low-frequency directivity performance. This not only reduces spatial aliasing but also enables the design of a very small microphone array module, that could potentially be installed directly in a class-1 measurement microphone e.g. with a 1/2″ capsule form factor.

8. REFERENCES

[1] D. Manvell and K. Andersen, "Developments in specific noise determination in continuous unattended monitoring systems," *Proc. of Euronoise 2018*, 2018.

[2] K. Zaman, M. Sah, C. Direkoglu, and M. Unoki, "A Survey of Audio Classification Using Deep Learning," *IEEE Access*, vol. 11, pp. 106620–106649, 2023, doi: 10.1109/access.2023.3318015.

[3] Z. Mnasri, S. Rovetta, and F. Masulli, "Anomalous sound event detection: A survey of machine learning based methods and applications," *Multimedia Tools and Applications*, vol. 81, no. 4, pp. 5537–5586, 2022.

[4] E. Betton-Ployon, A. Kacem, J. Mars, and N. Martin, "Enhanced railway sound event detection using YAMNet and classification criteria," *INTER-NOISE and NOISE-CON Congress and Conference Proc.*, vol. 270, no. 3, pp. 8834–8843, Oct. 2024, doi: 10.3397/in_2024_4148.

[5] K. H. Ejdfors, N. SATO, and L. A. SæLE, "A comparative study of noise event identification using AI in unattended monitoring," in *INTER-NOISE and NOISE-CON Congress and Conference Proc.*, 2024, pp. 7670–7678.

[6] D. T. Helboe and E. Fasting, "Automatic detection of source direction and exclusion of irrelevant sounds in unattended noise monitoring systems," *INTER-NOISE and NOISE-CON Congress and Conference Proc.*, vol. 268, no. 7, pp. 1131–1142, Nov. 2023, doi: 10.3397/in_2023_0172.

[7] E. Aflalo and T. Hupp, "Unattended noise measurements: use of new technologies to automatically qualify noise events for greater efficiency, precision and time savings," *Internoise 2024*, 2024.

[8] R. N. Miles, M. Farahikia, S. Leahy, and A. A. Aziz, "A flow-sensing velocity microphone," in *2019 IEEE SENSORS*, IEEE, Oct. 2019. doi: 10.1109/sensors43011.2019.8956947.

[9] Soundskrit Inc., "SKR0410 - PDM Directional Microphone Datasheet," 2023.

[10] A. Nehorai and E. Paldi, "Acoustic vector-sensor array processing," *IEEE Transactions on Signal Processing*, vol. 42, no. 9, pp. 2481–2491, 1994, doi: 10.1109/78.317869.

[11] J. Zhou and R. N. Miles, "Sensing fluctuating airflow with spider silk," *Proc. of the National Academy of Sciences*, vol. 114, no. 46, pp. 12120–12125, Oct. 2017, doi: 10.1073/pnas.1710559114.

[12] J. Zhou and R. N. Miles, "Directional Sound Detection by Sensing Acoustic Flow," *IEEE Sensors Letters*, vol. 2, no. 2, pp. 1–4, Jun. 2018, doi: 10.1109/lsens.2018.2843376.

[13] R. Miles, "Most animals hear acoustic flow instead of pressure; we should too," *The Journal of the Acoustical Society of America*, vol. 145, no. 3_Supplement, p. 1698, Mar. 2019, doi: 10.1121/1.5101224.

[14] P. Majdak, P. Balazs, and B. Laback, "Multiple exponential sweep method for fast measurement of head-related transfer functions," *Journal of the Audio Engineering Society*, vol. 55, no. 7/8, pp. 623–637, 2007.

[15] R. Schmidt, "Multiple emitter location and signal parameter estimation," *IEEE Transactions on Antennas and Propagation*, vol. 34, no. 3, pp. 276–280, doi: 10.1109/TAP.1986.1143830.

[16] "ANSI S1.11-2004: Specification for Octave-Band and Fractional-Octave-Band Analog and Digital Filters." New York, NY, 2004.